



A Comparison of Simulated *JWST* Observations Derived from Equilibrium and Non-equilibrium Chemistry Models of Giant Exoplanets

Sarah D. Blumenthal^{1,2,3} , Avi M. Mandell¹ , Eric Hébrard^{1,3} , Natasha E. Batalha^{1,4} , Patricio E. Cubillos⁵ , Sarah Rugheimer⁶ , and Hannah R. Wakeford¹

¹ NASA Goddard Space Flight Center, Center for Astrobiology, Greenbelt, MD 20771, USA; sarah.d.blumenthal@nasa.gov

² University of Maryland Baltimore County, CRESST, Baltimore, MD 21250, USA

³ Astrophysics Group, School of Physics, University of Exeter, Stocker Road, Exeter EX4 4QL, UK

⁴ Department of Astronomy and Astrophysics, Pennsylvania State University, State College, PA 16801, USA

⁵ Space Research Institute, Austrian Academy of Sciences, Schmiedlstraße 6, A-8042 Graz, Austria

⁶ School of Geography and Geosciences, University of St Andrews, St Andrews, UK

Received 2017 April 5; revised 2017 October 19; accepted 2017 November 27; published 2018 January 31

Abstract

We aim to see if the difference between equilibrium and disequilibrium chemistry is observable in the atmospheres of transiting planets by the *James Webb Space Telescope* (*JWST*). We perform a case study comparing the dayside emission spectra of three planets like HD 189733b, WASP-80b, and GJ 436b, in and out of chemical equilibrium at two metallicities each. These three planets were chosen because they span a large range of planetary masses and equilibrium temperatures, from hot and Jupiter-sized to warm and Neptune-sized. We link the one-dimensional disequilibrium chemistry model from Venot et al. (2012), in which thermochemical kinetics, vertical transport, and photochemistry are taken into account, to the one-dimensional, pseudo line-by-line radiative transfer model, *Pyrat bay*, developed especially for hot Jupiters, and then simulate *JWST* spectra using *PandExo* for comparing the effects of temperature, metallicity, and radius. We find the most significant differences from 4 to 5 μm due to disequilibrium from CO and CO₂ abundances, and also H₂O for select cases. Our case study shows a certain “sweet spot” of planetary mass, temperature, and metallicity where the difference between equilibrium and disequilibrium is observable. For a planet similar to WASP-80b, *JWST*’s NIRSpec G395M can detect differences due to disequilibrium chemistry with one eclipse event. For a planet similar to GJ 436b, the observability of differences due to disequilibrium chemistry is possible at low metallicity given five eclipse events, but not possible at the higher metallicity.

Key words: astrochemistry – planets and satellites: atmospheres – planets and satellites: composition – planets and satellites: gaseous planets

1. Introduction

The total exoplanet count currently exceeds 3000, and more than 700 orbit stars with a *J* magnitude between 6 and 12 (<http://exoplanets.org>). This subset represents optimal targets for observation with *The James Webb Space Telescope* (*JWST*) because their stellar fluxes do not saturate the detectors in standard time-series modes, and are therefore prime candidates for exploring composition and structure of exoplanet atmospheres. Now, we are entering the era of *JWST*, which will revolutionize the characterization of exoplanet atmospheres. Launching early to mid 2019, *JWST* is equipped with a 6.5 m primary mirror and large wavelength coverage from 0.6 to 28 μm with three near-infrared instruments and one mid-infrared instrument. Each observing mode offers higher spectral resolving power ($R=100\text{--}2700$) as compared to current space-based facilities ($R<100$).

The optimistic lifetime of *JWST* is 10 years, determined by its supply of on-board fuel. The current state-of-the-art space telescope, the *Hubble Space Telescope* (*HST*), is estimated to be decommissioned some time in 2020, making the operational lifetime of this serviceable telescope 30 years (since its launch in 1990). Due to the limited lifetime of *JWST* in contrast to *HST*, it is important that the community exploits the full potential of *JWST* as early as possible to produce a high scientific yield to expand our current understanding, to strongly motivate the commissioning of future space-based telescopes, and provide clear improvements for the continued creation of

these types of missions, such as the *Wide-Field Infrared Survey Telescope* and the *Large UV/Optical/Infrared Surveyor*. However, determining the best strategy for utilizing time with *JWST* is unclear, as mentioned in Stevenson et al. (2016). Stevenson et al. (2016) identified WASP-62b as a promising target for Early Release Science with *JWST*. This target has a high signal-to-noise ratio and an effective temperature ~ 1400 K. As this is relatively hot, it would be expected that the chemistry of this planet would be dominated by thermochemical equilibrium. For lower temperatures, however, it would be expected that the chemistry of a planet would be out of equilibrium. This is seen in our own solar system.

Much of our early understanding of the chemical composition of the atmospheres of highly irradiated exoplanets was gleaned using the assumption of chemical equilibrium. From the precedent set by earlier work (Burrows et al. 1997; Burrows & Sharp 1999; Seager & Sasselov 2000; Lodders & Fegley 2002; Burrows et al. 2008; Showman et al. 2009), equilibrium chemistry has become a widely used module in the analysis of exoplanet atmospheres. Most thermochemical equilibrium models employ a Gibbs’ free energy minimization strategy of iterating over adjustments of chemical abundance using thermodynamic data to achieve convergence. Studies have frequently concluded that disequilibrium processes could aid in a better interpretation of observational data, for example, Fortney et al. (2006), Showman et al. (2009), and Fortney et al. (2010). This motivated the development of more sophisticated

chemistry models that consider reaction timescales, chemical kinetics, and photochemistry (Liang et al. 2003; Cooper & Showman 2006; Zahnle et al. 2009; Line et al. 2010; Moses et al. 2011; Venot et al. 2012, 2016). Additionally, Baraffe (2014) discusses the brown dwarf, cousin to giant exoplanets, and points out the importance of non-equilibrium chemistry in brown dwarfs.

In this study, we focus on the impact of disequilibrium chemistry on the abundances of molecular species in the atmospheres of planets that may be observable by *JWST*. We choose to base our planetary parameters on several known transiting planets likely to be observed with *JWST*, spanning a range in planetary size and effective temperature (effectively signal-to-noise ratio) from hot Jupiter to warm sub-Neptune. We develop models based on the bulk properties of several well-known transiting planets, HD 189733b, WASP-80b, and GJ 436b. We explore the effect of metallicity assuming two different metallicities. The well-known planets HD 189733b and GJ 436b are chosen as representative bookends of our study. We chose the intermediate target WASP-80b because it has been described as the “missing link” in Triaud et al. (2015), as it receives the same flux as GJ 436b at $3.6\ \mu\text{m}$ (Triaud et al. 2015) but has a radius similar to that of Jupiter. Additionally, because WASP-80b has moderate temperatures ($\sim 800\ \text{K}$) and its host star exhibits strong chromospheric activity, it is an excellent target for studying disequilibrium chemistry effects. Thus, the goal of this study is to begin to define a regime where distinguishing disequilibrium chemistry from equilibrium chemistry may be possible.

2. Method

For the first time, we link together the equilibrium and disequilibrium chemistry models of Venot et al. (2012) to the open-source radiative transfer code *Pyrat Bay* and then to the open-source *JWST* simulator *PandExo* to simulate 1D globally-averaged secondary eclipse spectra at *JWST* resolution. It is the first study of its kind to compare disequilibrium and equilibrium chemistry on synthetic *JWST* spectra.

We chose to conduct our study in 1D rather than in 3D in order to explore a broader parameter space of different radii, temperatures, and metallicities using a robust chemical scheme. Exploring this same parameter space in 3D would be very computationally expensive to employ such a detailed chemical scheme. However, we recognize that 1D has its limitations as a proxy for 3D. Fortney et al. (2010) shows that for HD 189733b transmission spectra, 1D is a good proxy for 3D, but for HD 209458b transmission spectra, 1D is not a good proxy due to the temperature contrast generated by the terminator region.

For our study, our overall modeling scheme is as follows:

1. For HD 189733b, we use the temperature–pressure (TP) profile from Moses et al. (2011). For WASP-80b and GJ 436b, we generate a TP profile using Parmentier et al. (2015) and heat the upper atmosphere according to the process outlined in Moses et al. (2011).
2. We solve for the altitude of each TP point from our profile assuming hydrostatic equilibrium.
3. We run the equilibrium chemistry model using the inputs of the calculated TP profile along with altitude, and metallicity.
4. We use the resultant chemical abundances from the equilibrium chemistry run as initial conditions and run the

disequilibrium chemistry model until it reaches a steady state.

5. We use the respective chemical abundance outputs from the equilibrium and disequilibrium chemistry runs as inputs into the radiative transfer model, *Pyrat Bay*, and produce high-resolution emission spectra.
6. We use the high-resolution spectra as inputs into the *JWST* simulator, *PandExo* to produce simulated *JWST* spectra.

The specifics of each of these steps is explained in the following sections.

2.1. TP Profiles

For our study, we use 1D globally averaged TP profiles for the sake of inter-comparison with the profile from the well-studied planet of HD 189733b. The TP profile for HD 189733b is taken from Moses et al. (2011; also seen in Venot et al. 2012). This profile is derived from both a 1D globally-averaged profile from Fortney et al. (2006, 2010) and 3D global circulation models (GCM) from Showman et al. (2009; see Moses et al. 2011 for details). Additionally, Moses et al. (2011) heats the upper atmosphere of this TP profile, describing the addition of this heating as an “ad hoc” procedure, adapted from the results of Yelle (2004), García Muñoz (2007), and Koskinen et al. (2010). Koskinen et al. (2010) models of the upper atmosphere for HD 209458b, and calculates the lower boundary of its thermosphere as $\sim 0.1\ \mu\text{bar}$. Moses et al. (2011) employs this same pressure boundary for the TP profile of HD 189733b despite the differences in gravity ($9.4\ \text{m s}^{-2}$ for HD 209458b, $22.8\ \text{m s}^{-2}$ for HD 189733b), as the gravity affects the scale height and ultimately the location of this boundary. It is important to note that the foundational work on aeronomy in giant gas exoplanets was conducted in Yelle (2004) on globally-averaged TP profiles, citing the use of 1D in lieu of 3D models for the modeling of Titan’s atmosphere as a valid approach (Müller-Wodarg et al. 2000). For the sake of consistency, we apply the same heating procedure as Moses et al. (2011) to the profiles of WASP-80b and GJ 436b. The TP profiles for WASP-80b and GJ 436b are generated by the non-gray analytical model of Parmentier & Guillot (2014), assuming global redistribution ($\alpha = 0.25$) as 3D GCM results for these planets are unavailable. These TP profiles do not include any upper atmosphere heating so we apply the same heating procedure as that in Moses et al. (2011) to the profiles of WASP-80b and GJ 436b again ignoring the differences in gravity ($15.8\ \text{m s}^{-2}$ for WASP-80b, $12.6\ \text{m s}^{-2}$ for GJ 436b). The addition of this heating is achieved by cross-correlation to the TP profile of HD 189733b from Moses et al. (2011) for pressures of less than $0.1\ \mu\text{bar}$. The TP profiles used in our study are not calculated self-consistently.

For the calculation of scale height, we assume hydrostatic equilibrium, using a mean molecular weight of 2.3 for HD 189733b and WASP-80b, and 4.6 for GJ 436b (Line & Parmentier 2016).

We use the same eddy diffusion profile originally calculated in Moses et al. (2011) for all three planets. Moses et al. (2011) calculates a globally-averaged eddy diffusion profile from the 3D results of Showman et al. (2009). Little is known about eddy diffusion (as mentioned in Moses et al. 2011) thus, we choose to employ this calculated profile rather than a constant in an attempt to employ the state-of-the-art in eddy diffusion.

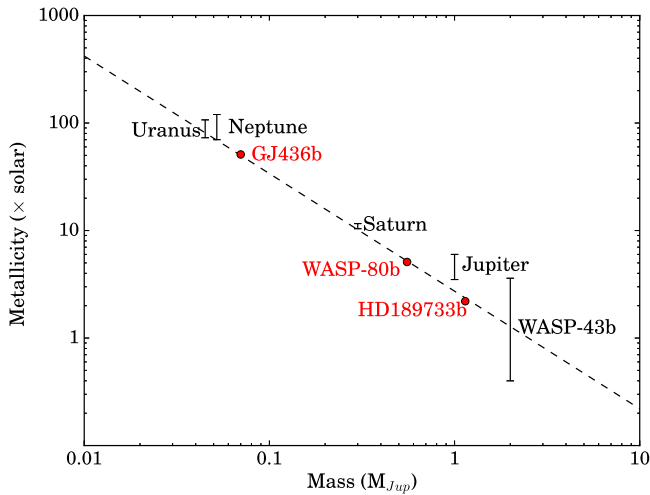


Figure 1. Planets analyzed in this paper used metallicities calculated from the solar system derived metallicity assumption seen in Kreidberg et al. (2014; dashed line); figure adapted directly from Kreidberg et al. (2014) with planets in this study in red.

Although the use of different eddy diffusion profiles for different planets could change our results, we instead aim to study the impacts of radius, temperature, and metallicity on the observability of disequilibrium with *JWST*. Thus, to study these parameters, we employ the same eddy diffusion profile (Moses et al. 2011) throughout our study to isolate these parameter. The sensitivity of eddy diffusion on calculated chemical composition is discussed in Moses et al. (2011).

2.2. Chemistry Models and Bulk Composition

For bulk composition, we investigate the effect of metallicity by comparing two different metallicities. We compare solar metallicity and the metallicity derived from the mass–metallicity relationship described in Kreidberg et al. (2014; now to be referred to as Kr14), where we scale from the solar abundance from Asplund et al. (2009; see Figure 1 and Table 1). We adopt the Kr14 metallicity for the “enriched” case as a unifying convention as the metallicity has been explored for HD 189733b and GJ 436b, but not for WASP-80b. We do not take into account the uncertainty in the Kreidberg-derived metallicity, but simply use metallicities that fall directly on the Kreidberg-fitted line. We input both solar and Kr14 metallicities into the equilibrium chemistry model. This elemental abundance is then propagated through to the disequilibrium chemistry model.

We use two chemistry models—one that models thermochemical equilibrium, which we call equilibrium for short, and one that models chemical kinetics with photochemistry, which we call disequilibrium. Our equilibrium chemistry model minimizes the Gibbs energy following the algorithm of Gordon & McBride (1994), adopting the same thermochemical data as Venot et al. (2012) in the form of NASA polynomial coefficients (McBride et al. 1993). Our disequilibrium chemistry model is a classical one-dimensional model of planetary atmospheres in which thermochemical kinetics, vertical transport, and photochemistry are taken into account. A nonlinear system of first-order ordinary differential equations (ODE) discretized along a vertical column of atmosphere is integrated as a function of time. It starts from an initial composition, using a backward differentiation formula implicit method for stiff problems implemented in the Fortran solver DLSODES within

the ODEPACK package (Hindemarch 1983; Radhakrishnan & Hindemarch 1993). Thermochemical kinetics rely on a chemical network consisting of 102 neutral species composed of C, H, N, and O linked by 1918 chemical reactions, that has been validated in the area of combustion chemistry by numerous experiments over the 300–2500 K temperature range and the 0.01–100 bar pressure regime. This has been found to be suitable to model the atmospheres of hot Jupiters (see Venot et al. 2012). Most reactions are reversed with their rate constants fulfilling detailed balance to ensure that thermochemical equilibrium is achieved at sufficiently long times in the absence of any disequilibrium processes (e.g., photochemistry and vertical transport).

Absorption and photodissociation cross sections are also taken from Venot et al. (2012). The different incident UV fluxes adopted follow the stellar models from Rugheimer et al. (2013) and Rugheimer et al. (2015), detailed in Table 1. The resulting UV fields in the atmospheres are calculated in spherical geometry for a 45° zenith angle after attenuation by both absorption and Rayleigh scattering (through a two-ray iterative algorithm; Isaksen et al. 1977). The ODE system is integrated from a chemical composition calculated at thermochemical equilibrium, with different elemental abundances (Asplund et al. 2009; Kreidberg et al. 2014) and the TP profile, discussed in Section 2.1.

2.3. Spectra Generator

To model the planetary emission spectra, we use the Python Radiative-transfer in a Bayesian framework package, *Pyrat Bay* (P. E. Cubillos et al. 2018, in preparation). *Pyrat Bay* is an open-source, reproducible package⁷ that is updated from the Bayesian Atmospheric Radiative Transfer package (Blecic 2016; Cubillos 2016).

Pyrat Bay solves the one-dimensional radiative-transfer equation, using the input atmospheric models (pressure, temperature, altitude, and abundances profiles), assuming a plane-parallel geometry. The code computes the emergent intensity spectra for a range of angles with respect to the normal. It then integrates the contribution from the different angles to produce the dayside flux spectrum. The radiative-transfer equation considers both absorption and emission from the atmosphere, adopting local-thermodynamic equilibrium to approximate the source function as the Planck function.

We consider the opacities from the expected major species in gas-giant planets. We incorporate molecular opacities from the “line-by-line” HITRAN and HITEMP databases (Rothman et al. 2013, 2010), see Table 2; the collision-induced absorption opacities for H₂–H₂ (Borysow et al. 2001; Borysow 2002) and H₂–He (Borysow et al. 1988, 1989; Borysow & Frommhold 1989); and Rayleigh scattering opacity (Lecavelier Des Etangs et al. 2008). Our calculation is done at a resolution of 1 cm^{−1}.

All inputs and outputs for our *Pyrat Bay* runs can be found at https://github.com/sdb05c/FiLeS_EQNEQ.

2.4. JWST Simulator

We use *PandExo* (Batalha et al. 2017)⁸ to simulate secondary eclipse observations of planets akin to HD 189733b, WASP-80b, and GJ 436b. We chose to simulate

⁷ <https://pcubillos.github.io/pyratbay/>

⁸ <https://github.com/natashabatalha/PandExo>

Table 1
Summary of Planets

Planet	R_p (R_{Jupiter})	M_p (M_{Jupiter})	Kreidberg Metallicity	T_{eff} (K)	T_{star} (K)	Stellar Type	Stellar Age	J magnitude	Stellar Model
HD 189733b	1.138	1.142	2	1191	4875	K1-K2	$>6 \times 10^8$ years	6.07	Eps Eridani ^a
WASP-80b	0.952	0.554	5	814	4150	K7V	unknown	9.22	BY Dra ^a
GJ436b	0.38	0.007	50	712	3684	M2.5	6.0 (± 5.0) Gyr	6.99	GJ 436 ^b

Notes.

^a From Rugheimer et al. (2013).

^b From Rugheimer et al. (2015).

Table 2
Molecular Opacity Sources

Molecule	Database	Spectral Coverage (cm^{-1})	Number of Lines
H ₂ O	HITEMP	0–30,000	114,241,164
CO ₂	HITEMP	258–9648	11,193,608
CO	HITEMP	3–8465	113,631
NO	HITEMP	0–9274	115,610
N ₂ O	HITRAN	0–7797	47,843
CH ₄	HITRAN	0–9200	290,091
O ₂	HITRAN	0–15,928	6428
NO	HITRAN	0–9274	105,079
NO ₂	HITRAN	0–3075	104,223
NH ₃	HITRAN	0–5295	29,084
H ₂ CO	HITRAN	0–3100	37,050
HCN	HITRAN	0–3424	4253
H ₂ O ₂	HITRAN	0–1731	126,983
C ₂ H ₂	HITRAN	604–9890	11,340
C ₂ H ₆	HITRAN	706–3001	22,402
C ₂ H ₄	HITRAN	701–3243	18,378

spectra using the Near-Infrared Imager and Slitless Spectrograph’s Single Object Slitless Spectroscopy mode (NIRISS SOSS; Doyon et al. 2012) from 0.6 to 2.8 μm ($R = 700$), Near InfraRed Spectrograph’s Grism 395 Medium Resolution mode (NIRSpec G395M; Birkmann et al. 2016) from 2.9 to 5 μm ($R = 1000$), and the Mid-Infrared Instrument’s Low Resolution Spectrometer (MIRI LRS; Kendrew et al. 2015; Rieke et al. 2015) from 5 to 14 μm ($R = 100$).

These observing modes were chosen because they offer nearly full wavelength coverage from 1 to 12 μm . NIRCам Grism with F322W2 and F444W2 could theoretically be used instead of NIRSpec G395M. Using these two NIRCам modes would decrease the noise in the 4–5 μm range but at the cost of 2 \times the observing time. The NIRSpec Prism, which offers wavelength coverage from 1 to 5 μm , cannot be used for HD 189733, WASP-80, or GJ 436 because all three planet systems are past the Prism’s saturation limit.

In the calculation of noise, PandExo does not assume a systematic noise floor. Greene et al. (2016) have suggested, based on previous observations with *HST* and *Spitzer*, that the noise floor for *JWST* might be 20–50 ppm. This will not be truly known until well after commissioning of the telescope. The assumption to not include a noise floor does not change the conclusions presented here.

PandExo uses the Phoenix Stellar Atlas models (Husser et al. 2013). Each transit observation consists of equal time spent in and out of transit (total time = 2 \times transit duration). HD 189733 and GJ 436 are at the saturation limits of the instruments and their observations for two groups/integrations, which correspond to a duty cycle of 0.33. WASP-80, with a $J = 9.22$, is well away from the saturation limit of NIRISS,

NIRSpec G395M, and MIRI, and therefore can be observed with a much higher efficiency (14 groups/integrations and a duty cycle of 0.86).

3. Results and Discussion

We examine the impacts of metallicity, temperature, and radius on the observability of disequilibrium chemistry in the atmospheres of our model planets with *JWST*. First, we present results showing the divergences from chemical equilibrium, assuming either solar metallicity (1 \times), or a Kr14 metallicity. We examine the resultant chemical abundances seen in Figure 2. As previously shown in Moses et al. (2011) and Venot et al. (2012) for a solar metallicity, a lower equilibrium temperature leads to a greater divergence from chemical equilibrium. Our results confirm this as well. Overall, we see more divergence from equilibrium in our GJ 436b-like planet than in our HD 189733b-like planet. This is because the lower the ambient temperature (and pressure), the slower the rate at which reactions will take place, thus causing the atmosphere to be farther away from equilibrium. When comparing close metallicities for the HD 189733b-like planet (1 \times and 2 \times), the computed abundances are nearly identical. See Venot et al. (2012) for a complete discussion on the chemical divergences from equilibrium for each species. Our WASP-80b-like planet, which has a equilibrium temperature 400 K colder than HD 189733b, shows larger divergences from chemical equilibrium. For both 1 \times and 5 \times solar metallicity, we see similar functions of abundance versus pressure; however, for the 5 \times solar metallicity case, as there are more “metals” available, so overall, molecules are in higher fraction. CO, CO₂, and NH₃ show the most divergence, and CH₄ has large divergence at low pressure. For the GJ 436b-like planet, it is similar to the WASP-80b-like planet in that we see again the most significant divergences in CO, CO₂, and NH₃, and large divergence for CH₄ at low pressures. For the 50 \times solar case, molecules are again in higher fraction as the availability of “metals” is higher than in the solar metallicity case. We see a larger magnitude of divergence for the solar metallicity case than in the 50 \times solar metallicity case.

It is also important to mention the quenching in each of these cases. We can see more species being clearly quenched in the WASP-80b-like and GJ 436b-like planet cases—CO, H₂O, CH₄, NH₃, CO₂, and HCN—than in the HD 189733b-like planet cases. In the HD 189733b-like planet case, we only see CO and H₂O being clearly quenched. However, the quenching behavior of HCN in the HD 189733b-like cases is similar to the HCN quenching behavior in the WASP-80b-like cases. Additionally, it is important to note that the very slight divergence from equilibrium water undergoes in the Kr14 metallicity cases. As the metallicity increases and the temperature decreases, we see more divergence.

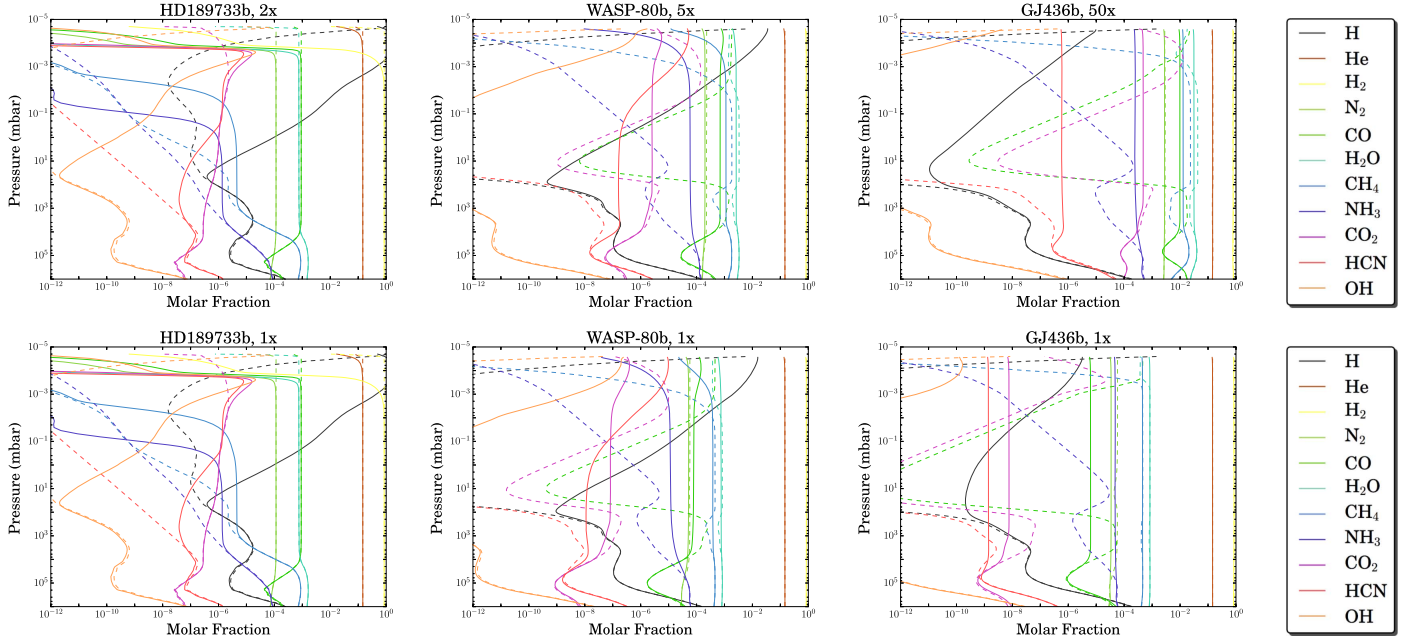


Figure 2. Equilibrium (dashed lines) vs. disequilibrium (solid lines) chemical abundances for solar metallicity (top row) and Kr14 metallicity (bottom row) for planets like HD 189733b, WASP-80b, and GJ 436b.

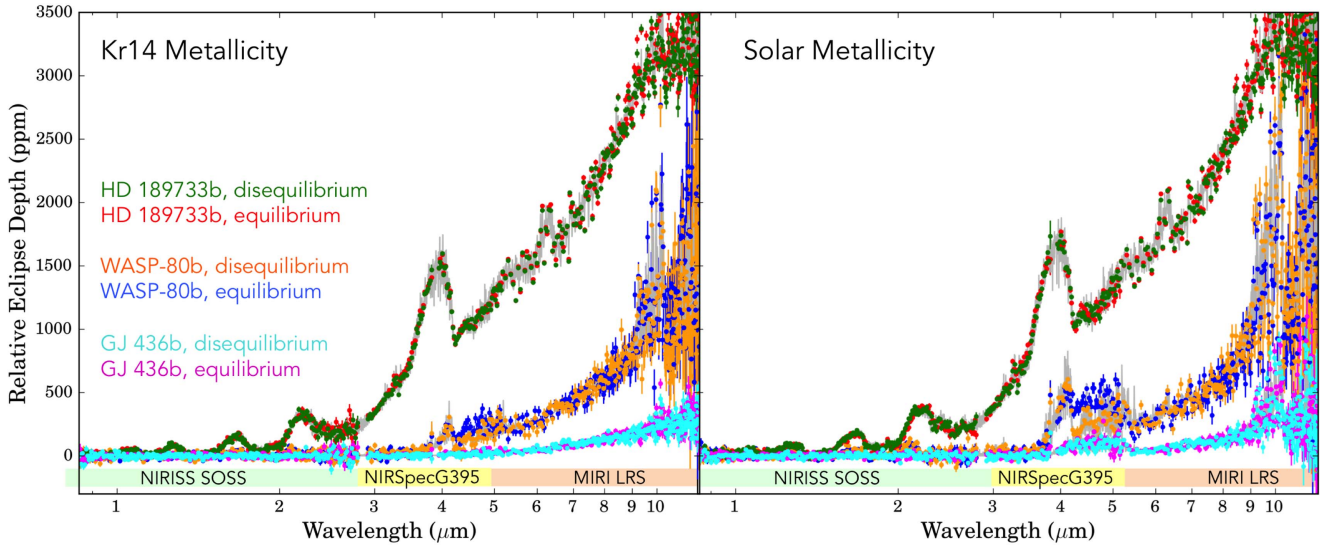


Figure 3. *JWST* simulated spectra for the three planets for five eclipse events at an $R = 100$. HD 189733b equilibrium and disequilibrium, respectively, in red and green, WASP-80b in blue and orange, GJ 436b in magenta and cyan. Left shows Kreidberg-derived (Kr14) metallicity, and right shows solar metallicity for the three *JWST* instruments. The disequilibrium model spectra is underplotted in light gray.

Using the equilibrium and non-equilibrium abundances shown in Figure 2 as inputs, we examine the impacts of metallicity, radius, and temperature on the observability of non-equilibrium chemistry processes in the atmospheres of our planets with *JWST*'s NIRISS SOSS, NIRSpec G395M, and MIRI LRS (Figure 3). Our criteria for observability is defined as a difference in a single-bin eclipse depth of greater than 60 ppm in the NIR and 150 ppm in the MIR; this would be a 3σ result based on expected noise floors for the *JWST* instruments (Greene et al. 2016). In order to distinguish between model spectra at a level above the noise contribution for each bin, we model the spectra seen in Figure 3, assuming a total of five eclipse events. Divergence between equilibrium and disequilibrium chemistry becomes observable from 4 to 5 μm using the NIRSpec G395M. We cannot disentangle equilibrium from

disequilibrium chemistry using NIRISS SOSS or MIRI LRS for any of our selected cases.

As seen in Figure 2, the largest chemical differences between equilibrium and disequilibrium compositions are in the GJ 436b-like planet, the coolest in our study. We expected these differences to be the most noticeable by *JWST* but, due to the radius of this planet, these differences are not as observable as those for the larger and slightly warmer WASP-80b-like planet. The magnitude of the observed flux and the magnitude of the difference between spectra from equilibrium and disequilibrium models is greater for solar metallicity planets than enriched planets. The difference between equilibrium and disequilibrium chemistry becomes observable from 4 to 5 μm for both metallicities for the WASP-80b-like planet and barely observable for the GJ 436b-like planet at solar metallicity, but

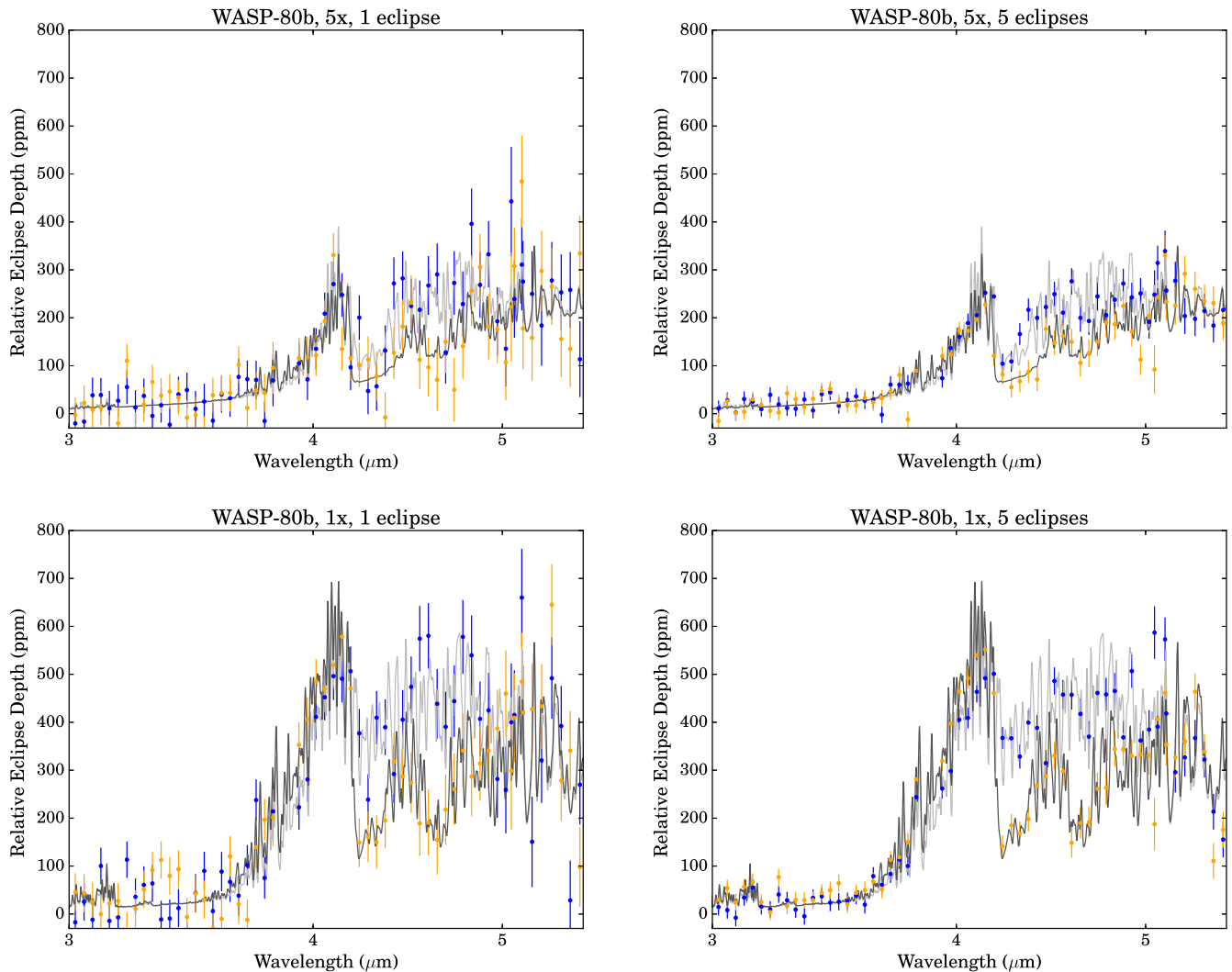


Figure 4. Zoomed region of *JWST* simulated spectra for the WASP-80b-like planet to highlight the observable differences seen from 4 to 5 μm at $R = 50$. Equilibrium chemistry points in blue, high-resolution model in light gray, and disequilibrium points in yellow, high-resolution spectra in darker gray. Modeled with (row 1) Kr14 metallicity ($5\times$) and (row 2) solar metallicity, for (left column) one eclipse event and (right column) five eclipse events.

not observable at $50\times$ solar metallicity. The average difference from 4 to 5 μm for a GJ 436b-like planet is 30 ppm for solar metallicity, which is only a 1.5σ result according to noise predictions made in Greene et al. (2016). The average difference from 4 to 5 μm for a WASP-80b-like planet is 60 ppm for $5\times$ solar metallicity, and 130 ppm for solar metallicity. As metallicity increases, the intensity of spectral features decreases. Thus the sweet spot from 4 to 5 μm also depends on metallicity. The difference in radii between WASP-80b and GJ 436b is $\sim 86\%$ (calculated from Table 1). We see no discernible differences for our HD 189733b-like planet at both solar and $2\times$ solar metallicities. The difference in radius between HD 189733b and WASP-80b is $\sim 18\%$ but the difference in temperature is $\sim 40\%$ (calculated from Table 1). Thus, this sweet spot is made up of the intersection of temperature, radius, and metallicity. It is important to note that these results are highly dependent on the fixed inputs presented and could or could not be discernible under different conditions.

As time observing with *JWST* is at an ultimate premium, we examine how a few events can be used to make this distinction in our study for the wavelength region from 4 to 5 μm . We also

choose to demonstrate the observability below native resolution ($R = 50$) for emphasis. In Figures 4 and 5, the spectra calculated assume one and five eclipse events for both metallicities of the WASP-80b-like and GJ 436b-like planets, respectively. As expected, the more events, the clearer the separation between equilibrium and disequilibrium in this region. For the WASP-80b-like planet (Figure 4), we can see the divergence after only one eclipse event. This divergence is clearer for the solar metallicity case than for the $5\times$ solar metallicity case. Thus, with five eclipse events, the difference between equilibrium and disequilibrium spectra is clear in this wavelength region. For the GJ 436b-like planet (Figure 5), we can only see this clear separation at solar metallicity and with five eclipses. There is too much noise to make the distinction between equilibrium and disequilibrium for one eclipse event at solar metallicity, and at high metallicity the distinction cannot be made at all. We choose to include this null result to show the effect of high metallicity. Here it is important to discuss the assumed metallicity for our GJ 436b-like planet. We assume a metallicity of $50\times$ solar, following Kreidberg et al. (2014), rather than a higher metallicity as reported in Moses et al. (2013). Moses et al. (2013) singularly study this planet and

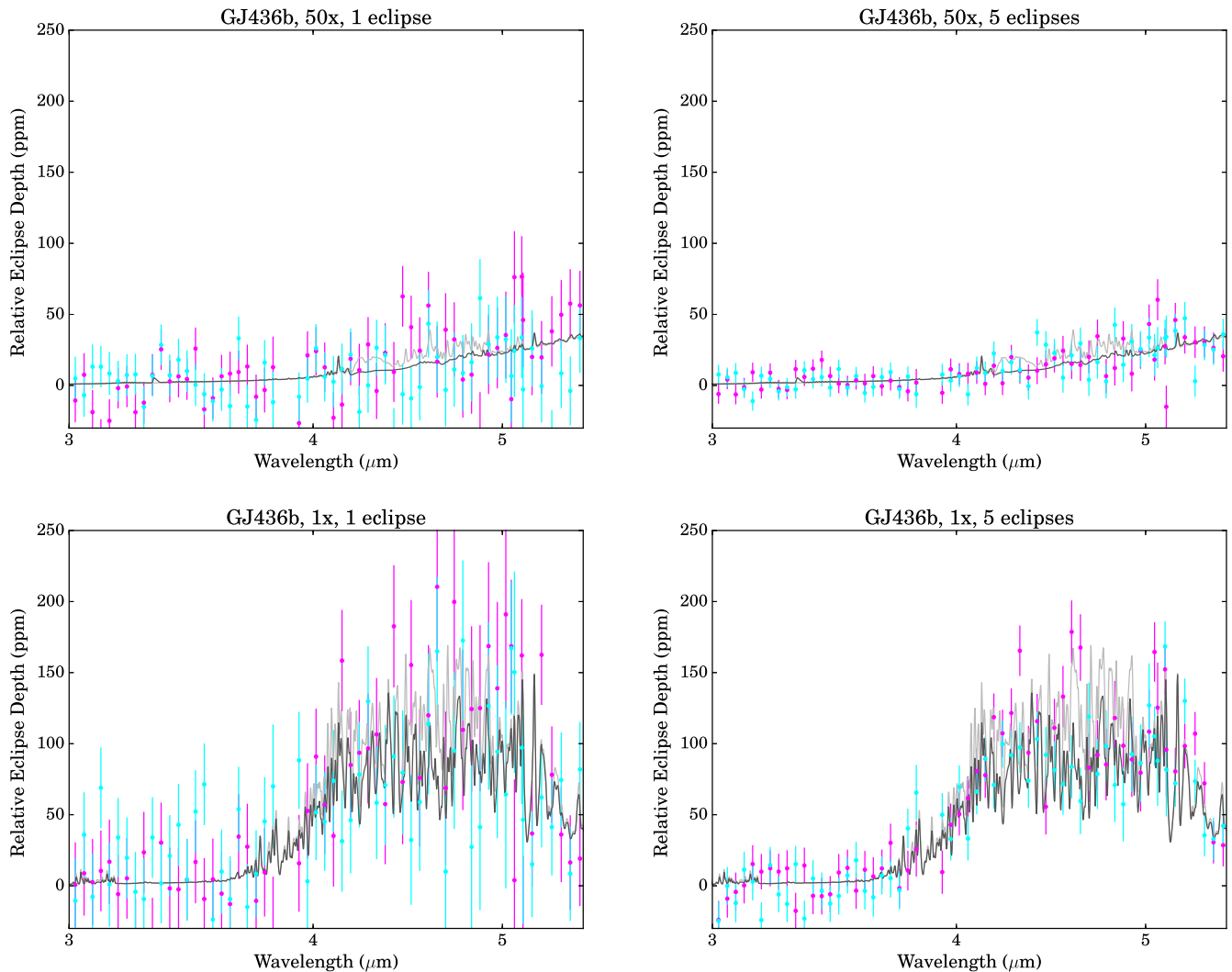


Figure 5. Zoomed region of *JWST* simulated spectra for the GJ 436b-like planet to highlight the observable differences seen from 4 to 5 μm at $R = 50$. Equilibrium chemistry points are in magenta, high-resolution model points are in light gray, and disequilibrium points are in cyan. Modeled with (row 1) Kr14 metallicity ($50\times$) and (row 2) solar metallicity, for (left column) one eclipse event and (right column) five eclipse events.

report metallicity values of ~ 230 – 2000 times solar. At these higher metallicities, we would also expect for the differences to be indistinguishable given the rest of our model inputs.

We investigate the chemical sources of the difference seen from 4 to 5 μm by analyzing each species’ contribution to the overall spectra. We discuss the contributions of individual species seen in Figures 6–8. Please note that the y-axis scale is kept consistent for each planet regardless of the metallicity case.

For the WASP-80b-like planet at solar metallicity, the spectral contributions from CO, CO₂, and H₂O predominantly comprise the overall disequilibrium and equilibrium spectra. For the disequilibrium chemistry case, the region from 4.2 to 4.4 μm is from CO₂, and the region from 4.4 to 5.0 μm is from CO. For the equilibrium case, the region from 4.3 to 5.0 μm is from H₂O. In Figure 6, the overall difference between equilibrium and disequilibrium for the individual species does not represent a complete census on which species are responsible for the difference seen in Figure 3 between 4.0 and 5.0 μm . Instead, the responsibility of this difference is from the relationship between these three species—CO, CO₂, and H₂O. We can see that the difference between equilibrium and

disequilibrium H₂O is small, but because water is so strongly absorbing, in the equilibrium case, its contribution masks the contributions of CO and CO₂. Thus, the difference we see between the overall equilibrium and disequilibrium spectra is from H₂O and disequilibrium CO and CO₂. In Figure 2, equilibrium CO and CO₂ are in less abundant than in disequilibrium—the largest divergence from equilibrium is around 10 mbar. As water abundance changes only slightly in the equilibrium and disequilibrium chemistry cases, the point at which water becomes optically thick is important, as it could mask or reveal the divergence from equilibrium for CO and CO₂.

Similar to the solar metallicity case for the WASP-80b-like planet, the $5\times$ metallicity planet (Figure 7), the contribution of disequilibrium CO₂ from 4.2 to 4.4 μm absorbs stronger than disequilibrium H₂O. However, for this metallicity case, both disequilibrium CO and H₂O are responsible for the 4.4–5.0 μm region of the disequilibrium spectrum region. For the overall equilibrium spectrum, CO₂ and CO graze the overall spectrum, but, in this region from 4.0 to 5.0 μm , the equilibrium spectrum is dominated by the contribution from equilibrium H₂O. In the difference plot in Figure 7, there is a larger difference between

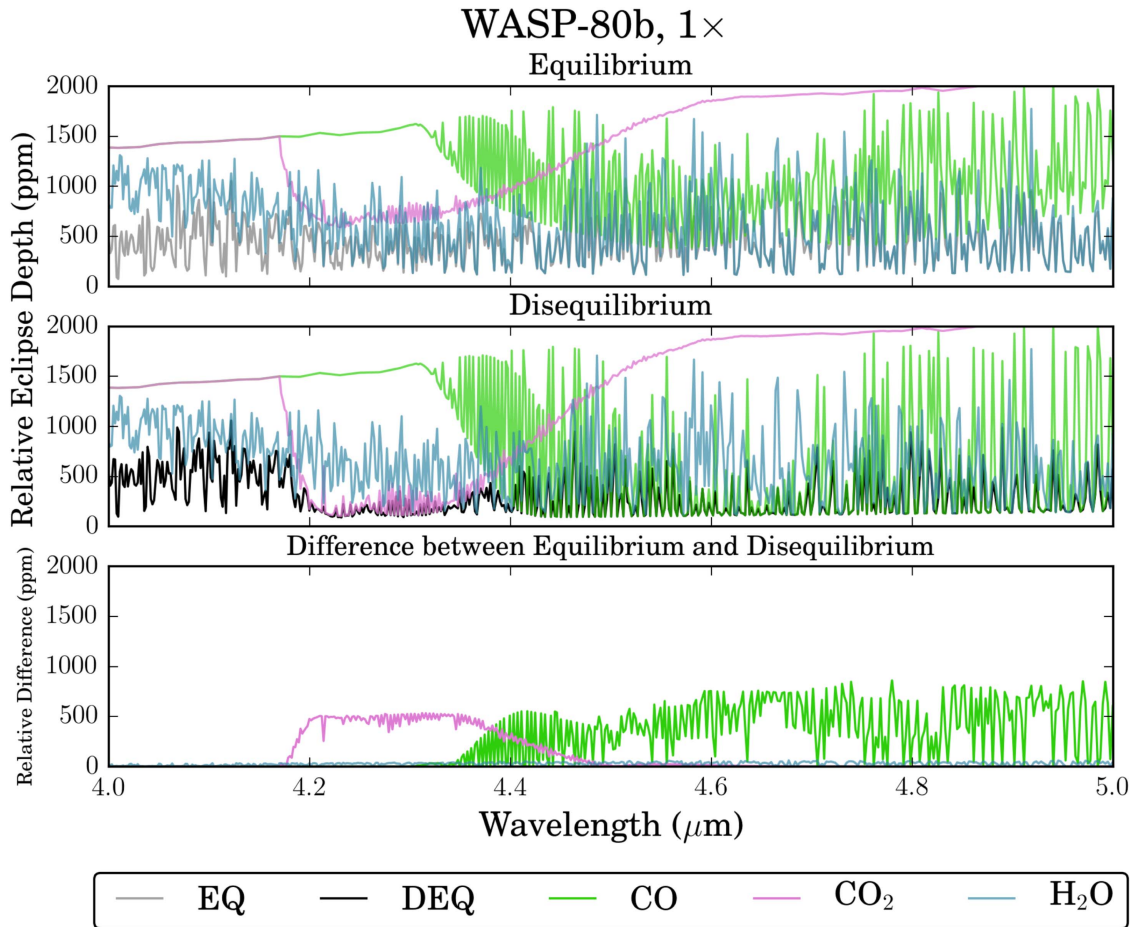


Figure 6. Individual spectral contributions of CO (green), CO₂ (pink), and H₂O (blue) from equilibrium chemistry (panel 1) and disequilibrium chemistry (panel 2) overlaid on the overall spectra of disequilibrium (dark gray) and equilibrium (light gray) chemistry cases for the WASP-80b-like planet at solar metallicity. Panel 3 plots the differences between the disequilibrium and equilibrium cases for the aforementioned molecules.

equilibrium and disequilibrium H₂O than at solar metallicity. Thus, the overall difference we see in Figure 3 between 4.0 and 5.0 μm is between disequilibrium CO₂, CO, and H₂O and equilibrium H₂O. As this is a higher metallicity case, there is more H₂O in the system than at solar metallicity, making the difference between equilibrium and disequilibrium more spectrally relevant.

We examine the individual species’ contributions for only the solar metallicity case of our GJ 436b-like planet as the difference between equilibrium and disequilibrium for the 50 \times solar metallicity case is not observable. For this planet, we have included the spectral contribution from CH₄ as it is relevant for this case but not for both metallicity cases of the WASP-80b-like planet. In Figure 8, from 4 to 4.4 μm the disequilibrium spectrum is dominated by disequilibrium CH₄, obscuring the contributions from H₂O and CO₂. For both disequilibrium and equilibrium, CO₂ is not expressed in the overall spectra. From 4.4 to 5.0 μm , disequilibrium CO dominates the overall disequilibrium spectrum. For the equilibrium spectrum, again CH₄ dominates the same region from 4.0 to 4.4 μm , and equilibrium H₂O dominates the rest of the equilibrium spectrum from 4.4 to 5.0 μm . In the difference plot in Figure 8, there are large differences for CO but not for H₂O or CH₄. Thus, the difference between equilibrium and disequilibrium from 4.0 to 5.0 μm in Figure 3 is between disequilibrium CO and equilibrium H₂O. The increased abundance of CO in disequilibrium impacts the observed overall spectra. From

Figure 2, we see large divergences from equilibrium for both CO and CO₂ centered at 10 mbar; however, because of the strong absorption from both CH₄ and H₂O, the spectral contribution from CO₂ is masked. Thus, similarly to the solar metallicity case of the WASP-80b-like planet, the point at which H₂O becomes optically thick will determine if the contribution from CO is masked or revealed in the overall observed spectra.

3.1. Further Discussion and Future Work

Burrows (2014) points out the “primitive” state of exoplanet data, and therefore how pinning down metallicity is difficult at this point. Burrows (2014) explains that only when higher resolution data across a large wavelength domain are available will we be able to start making better conclusions about metallicity. Due to the increase of resolution with *JWST*, it is important to take disequilibrium chemistry into account when determining metallicity. In particular, in this study, we see that the abundances of CO, CO₂, and H₂O are sensitive to disequilibrium chemistry and that their contributions create an observable difference between 4.0 and 5.0 μm . Madhusudhan & Seager (2011) point out that for their study of GJ 436b, chemical abundances cannot be fully explained using equilibrium chemistry, and therefore the metallicity cannot be determined using these equilibrium abundances. By taking disequilibrium

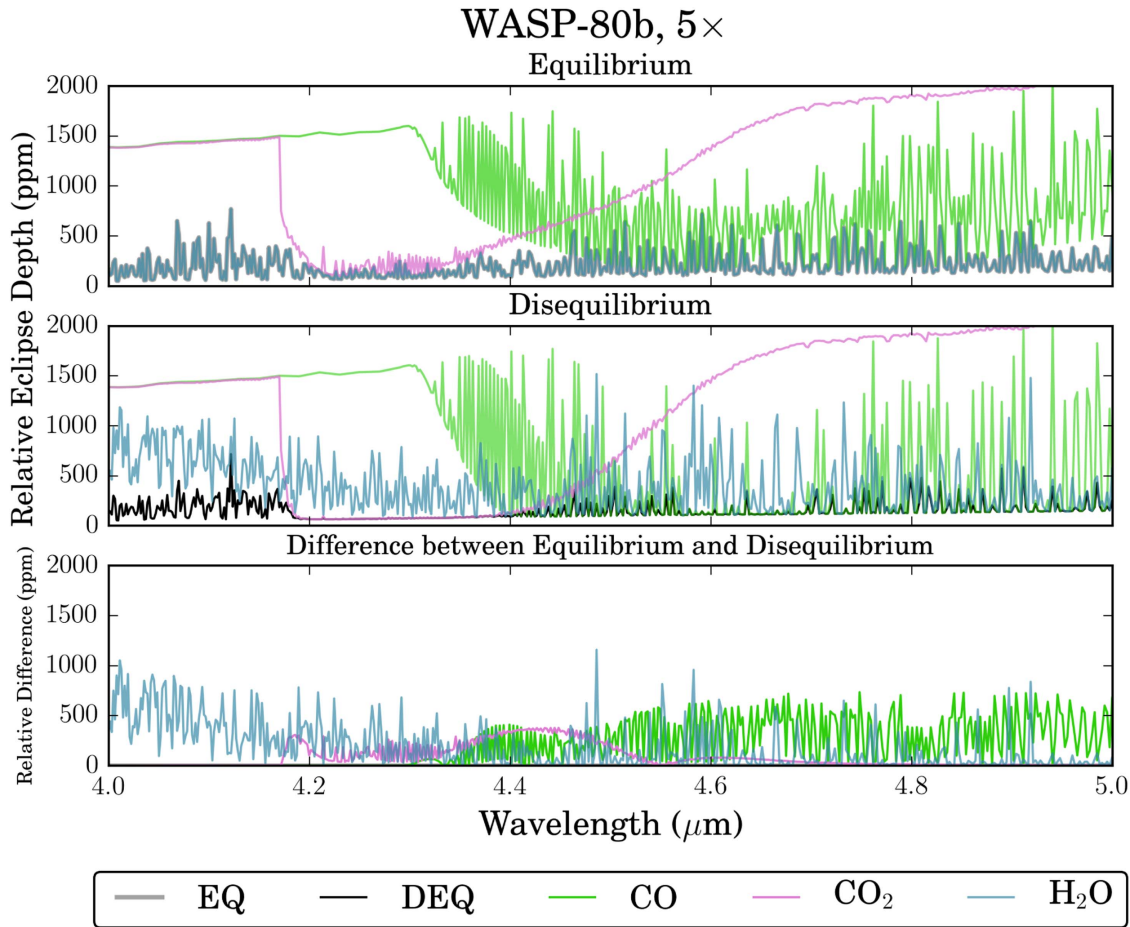


Figure 7. Individual spectral contributions of CO (green), CO₂ (pink), and H₂O (blue) from equilibrium chemistry (panel 1) and disequilibrium chemistry (panel 2) overlaid on the overall spectra of disequilibrium (dark gray) and equilibrium (light gray) chemistry cases for the WASP-80b-like planet at 5× metallicity. Panel 3 plots the differences between the disequilibrium and equilibrium cases for the aforementioned molecules.

chemistry (including photochemistry), we can better determine the metallicity of giant gaseous exoplanets.

We choose to model only two metallicities per planet—solar and Kr14 metallicity (as mentioned in Section 2). Kreidberg et al. (2014) suggest that atmospheric metallicity of giant gas planets in the solar system might be significantly higher than the stellar metallicity. The relationship derived in Kreidberg et al. (2014) uses CH₄ to derive solar system metallicities and H₂O for exoplanet metallicity. However, Guillot & Gautier (2015) point out that the molecular abundances and therefore bulk metallicity for solar system objects are notoriously hard to pin down. Guillot & Gautier (2015) also point out the vast progression over the mere last 10 years in constraining the Sun’s elemental composition; and the nonlinear divergence from solar metallicity in our own gas planets, reporting that in carbon alone it is enriched 4 fold in Jupiter, 10 fold in Saturn, and 90 fold in Neptune. Additionally, the Galileo probe found on Jupiter that carbon, nitrogen, and sulfur elemental abundances were supersolar between 2.5 and 4.5 times (Wong et al. 2004). As for oxygen, its elemental abundance is harder to constrain because water is so far out of equilibrium on Jupiter (and the probe fell into a hot presumably dry spot and did not finish its measurements). For exoplanet analysis, it has been a popular assumption to use solar metallicity (Cooper & Showman 2006; Fortney et al. 2006, 2008; Fortney 2007; Moses et al. 2011; Venot et al. 2012; Koskinen et al. 2013; Zahnle & Marley 2014; Wakeford & Sing 2015; Heng 2016;

Kataria et al. 2016; Barstow et al. 2017; Gao et al. 2017) or a linear scaling of solar metallicity (Freedman et al. 2014; Charnay et al. 2015; Kataria et al. 2015; Wakeford et al. 2017), which is why we chose to model it as one of our metallicity cases. The bulk composition of a planet’s atmosphere plays a major role in the chemistry at work in the planet’s atmosphere. The bulk composition of exoplanet atmospheres will depend on its formation history (Öberg et al. 2011; Madhusudhan et al. 2014; Wakeford et al. 2017). Wakeford et al. (2017) clearly demonstrate this with the analysis of HAT-P-26b, which departs from the Kr14 relationship. Thus, we recognize the limited metallicity space we have explored but have accomplished how disequilibrium chemistry should be taken into account when determining metallicity and how *JWST* may provide insight into this determination. Better understanding of our own giant planets’ nonlinear relationship with solar elemental abundance may help us to understand our own system’s formation. From there, we may be able to better diagnose the bulk composition of exoplanets and understand their formation. (The *Juno* mission is currently attempting to discern the H₂O abundance of Jupiter using gravitational and radar diagnostics.) Retrieval methods may benefit from exploring and/or iterating over a diverse set of scenarios for a planet’s bulk elemental abundances. We leave exploration of more metallicities including nonlinear scaling of solar elemental abundance for future studies that seeks to match observations.

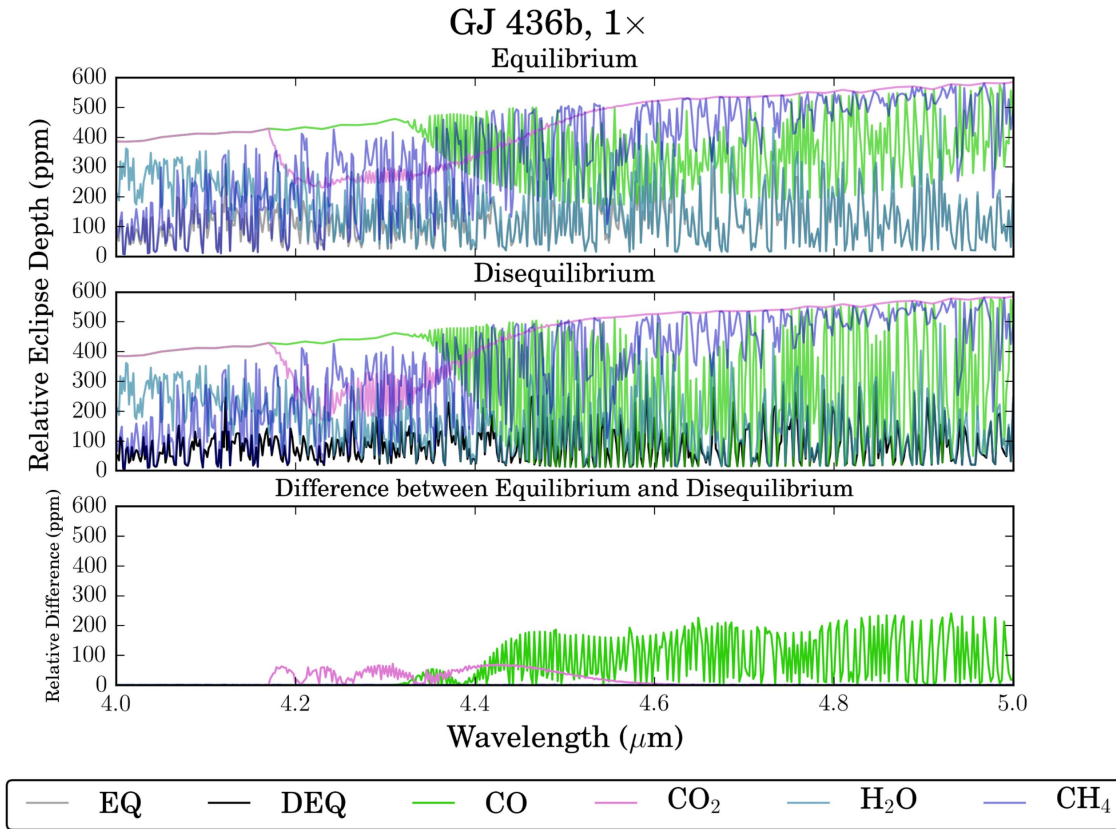


Figure 8. Individual spectral contributions of CO (green), CO₂ (pink), and H₂O (blue) from equilibrium chemistry (panel 1) and disequilibrium chemistry (panel 2) overlaid on the overall spectra of disequilibrium (dark gray) and equilibrium (light gray) chemistry cases for the GJ 436b-like planet at solar metallicity. Panel 3 plots the differences between the disequilibrium and equilibrium cases for the aforementioned molecules.

It is also important here to remark on the reliance of the abundances of CO, CO₂, or H₂O on the TP profile. As mentioned in Section 2, our TP profile is not calculated self-consistently. In order to isolate the differences between equilibrium and disequilibrium chemistry, we kept the TP profiles identical whereas consistently calculated profiles differ based on whether the chemistry is specified as in or out of equilibrium. Given the work of Drummond et al. (2016), which models TP profiles self-consistently in and out of equilibrium, the resultant TP profiles of HD 189733b would probably lie in between equilibrium and non-equilibrium (also called disequilibrium) chemistry profiles. Thus, as the profiles presented in this study are calculated analytically with no radiative feedback, our disequilibrium results would be affected. With self-consistently calculated TP profiles, our disequilibrium results would also probably lie somewhere in between our current equilibrium and disequilibrium results.

We recognize the limitations of a 1D study for accurate comparison with observations, but we utilize 1D here for rapid exploration of parameter space. There has been limited work employing chemical kinetics in 3D. Cooper & Showman (2006) study CO, CH₄, and H₂O in 3D with a limited chemical network, incorporating the chemical kinetic rate of only the rate-limiting reactions into the relaxation timescale. In between 1D and 3D is the work of Agúndez et al. (2014), which studies HD 189733b and HD 209458b in “pseudo 2D.” Agúndez et al. (2014) uses a robust chemical scheme and simplified dynamics to study the interplay between chemistry and dynamics. Again, we leave modeling chemical kinetics in 3D for future work that seeks to match observations.

Finally, the chemistry models we use in this study, though considered state-of-the-art, contain only gaseous species for carbon, nitrogen, and oxygen chemistry. As pointed out in Zahnle et al. (2009, 2016), the inclusion of sulfur-containing species is important, however, the reaction rates for these species at high temperature remain poorly constrained. Additionally, Fortney et al. (2016) points out that we also lack the optical data to interpret these sulfur-containing gases. It is crucial to point out that our study does not include haze or clouds and the results presented here could be seriously skewed without their inclusion (Morley et al. 2012, 2015; Wakeford & Sing 2015; Line & Parmentier 2016; Parmentier et al. 2016; Sing et al. 2016; Wakeford et al. 2017). Future, more realistic studies will include condensed phase chemistry.








4. Conclusions

In our study, we seek not to match observations, but to explore a limited parameter space to demonstrate the observability of disequilibrium chemistry with *JWST* in 1D. We provide a 1D study that for the first time links equilibrium versus disequilibrium chemistry to simulated *JWST* spectra. We find a sweet spot in radius ($>0.952 R_{\text{Jup}}$), metallicity (between $1\times$ and $5\times$ solar), and temperature ($<\sim 800$ K) for observing differences due to disequilibrium chemistry from 4 to $5\mu\text{m}$ with the NIRSpec G395M. We find that the spectral signature of an atmosphere in chemical disequilibrium can be distinguished from an atmosphere in chemical equilibrium for a planet like warm-Jupiter WASP-80b for the two input metallicity cases; but for the slightly cooler sub-Neptune GJ

436b, we find that we can only partially detect the contribution from disequilibrium chemistry in the case of solar metallicity but not for the $50\times$ solar metallicity case. We report that based on a select set of input parameters, CO, CO₂, and H₂O are responsible for differences in our WASP-80b-like and GJ 436b-like planet cases. Thus, as the signatures from CO and CO₂ are visible in the observed disequilibrium spectra, but not in equilibrium spectra, disequilibrium chemistry should be considered when determining the metallicity of a planet. We cannot observe disequilibrium chemistry in the HD 189733b-like planet given our inputs because it is too hot. At such high temperatures, thermochemical equilibrium dominates over disequilibrium processes.

S.D.B. would like to thank Ned Molter and Conor Nixon for meaningful conversations about hydrostatic equilibrium and Aarynn Carter for meaningful conversations about *JWST*. S.D.B. thanks NASA, GSFC, and UMBC for their support of this work and the University of Exeter for support through a Ph.D. studentship. Finally, S.D.B. would like to thank the referee whose comments greatly improved the manuscript.

ORCID iDs

Sarah D. Blumenthal  <https://orcid.org/0000-0002-3173-1637>
 Avi M. Mandell  <https://orcid.org/0000-0002-8119-3355>
 Eric Hébrard  <https://orcid.org/0000-0003-0770-7271>
 Natasha E. Batalha  <https://orcid.org/0000-0003-1240-6844>
 Patricio E. Cubillos  <https://orcid.org/0000-0002-1347-2600>
 Sarah Rugheimer  <https://orcid.org/0000-0003-1620-7658>
 Hannah R. Wakeford  <https://orcid.org/0000-0003-4328-3867>

References

- Agúndez, M., Parmentier, V., Venot, O., Hersant, F., & Selsis, F. 2014, *A&A*, **564**, A73
- Asplund, M., Grevesse, N., Sauval, A. J., & Scott, P. 2009, *ARA&A*, **47**, 481
- Baraffe, I. 2014, *Astrophysical and Space Science Library*, 401
- Barstow, J. K., Aigrain, S., Irwin, P. G. J., & Sing, D. K. 2017, *ApJ*, **834**, 50
- Batalha, N. E., Mandell, A., Pontoppidan, K., et al. 2017, *PASP*, **129**, 064501
- Birkmann, S. M., Ferruit, P., Rawle, T., et al. 2016, *Proc. SPIE*, **99040**, 99040B
- Blecic, J. 2016, PhD Dissertation (arXiv:1604.02692)
- Borysow, A. 2002, *A&A*, **390**, 779
- Borysow, A., & Frommhold, L. 1989, *ApJ*, **341**, 549
- Borysow, A., Frommhold, L., & Moraldi, M. 1989, *ApJ*, **336**, 495
- Borysow, A., Jorgensen, U. G., & Fu, Y. 2001, *JQSRT*, **68**, 235
- Borysow, J., Frommhold, L., & Birnbaum, G. 1988, *ApJ*, **326**, 509
- Burrows, A., Budaj, J., & Hubeny, I. 2008, *ApJ*, **678**, 1436
- Burrows, A., & Sharp, C. M. 1999, *ApJ*, **512**, 843
- Burrows, A. S. 2014, *PNAS*, **111**, 12601
- Burrows, A., Marley, M., Hubbard, W. B., et al. 1997, *ApJ*, **491**, 856
- Charnay, B., Meadows, V., & Leconte, J. 2015, *ApJ*, **813**, 15
- Cooper, C. S., & Showman, A. P. 2006, *ApJ*, **649**, 1048
- Cubillos, P. E. 2016, PhD Dissertation (arXiv:1604.01320)
- Doyon, R., Hutchings, J. B., Beaulieu, M., et al. 2012, *Proc. SPIE*, **8442**, 84422R
- Drummond, B., Tremblin, P., Baraffe, I., et al. 2016, *A&A*, **594**, A69
- Fortney, J. J. 2007, in ASP Conf. Ser. 366, *Transiting Extrapolar Planets Workshop*, ed. C. Afonso, D. Wel Drake, & T. Henning (San Francisco, CA: ASP), 297
- Fortney, J. J., Cooper, C. S., Showman, A. P., Marley, M. S., & Freedman, R. S. 2006, *ApJ*, **652**, 746
- Fortney, J. J., Lodders, K., Marley, M. S., & Freedman, R. S. 2008, *ApJ*, **678**, 1419
- Fortney, J. J., Robinson, T. D., Domagal-Goldman, S., et al. 2016, arXiv:1602.06305
- Fortney, J. J., Shabram, M., Showman, A. P., et al. 2010, *ApJ*, **709**, 1396
- Freedman, R. S., Lustig-Yaeger, J., Fortney, J. J., et al. 2014, *ApJS*, **214**, 25
- Gao, P., Marley, M. S., Zahnle, K., Robinson, T. D., & Lewis, N. K. 2017, *AJ*, **153**, 139
- García Muñoz, A. 2007, *P&SS*, **55**, 1426
- Gordon, S., & McBride, B. J. 1994, Computer Program for Calculation of Complex Chemical Equilibrium Compositions and Applications. I. Analysis, Reference Publication RP-1311 (Washington, D.C.: NASA)
- Greene, T. P., Line, M. R., Montero, C., et al. 2016, *ApJ*, **817**, 17
- Guillot, T., & Gautier, D. 2015, in *Treatise on Geophysics*, ed. T. Spohn & G. Schubert (2nd ed.; New York: Elsevier), 10.16
- Heng, K. 2016, *ApJL*, **826**, L16
- Hindemarch, A. C. 1983, in *IMACS Transactions on Scientific Computation*, ed. R. S. Stepleman (Amsterdam: North-Holland), 55
- Husser, T.-O., Wende-von Berg, S., Dreizler, S., et al. 2013, *A&A*, **553**, A6
- Isaksen, I. S. A., Midtbo, K. H., Sunde, J., & Crutzen, P. J. 1977, *GeoNr*, **31**, 11
- Kataria, T., Showman, A. P., Fortney, J. J., et al. 2015, *ApJ*, **801**, 86
- Kataria, T., Sing, D. K., Lewis, N. K., et al. 2016, *ApJ*, **821**, 9
- Kendrew, S., Scheithauer, S., Bouchet, P., et al. 2015, *PASP*, **127**, 623
- Koskinen, T. T., Harris, M. J., Yelle, R. V., & Lavvas, P. 2013, *Icar*, **226**, 1678
- Koskinen, T. T., Yelle, R. V., Lavvas, P., & Lewis, N. K. 2010, *ApJ*, **723**, 116
- Kreidberg, L., Bean, J. L., Désert, J.-M., et al. 2014, *ApJL*, **793**, L27
- Lecavelier Des Etangs, A., Pont, F., Vidal-Madjar, A., & Sing, D. 2008, *A&A*, **481**, L83
- Liang, M.-C., Parkinson, C. D., Lee, A. Y.-T., Yung, Y. L., & Seager, S. 2003, *ApJL*, **596**, L247
- Line, M. R., Liang, M. C., & Yung, Y. L. 2010, *ApJ*, **717**, 496
- Line, M. R., & Parmentier, V. 2016, *ApJ*, **820**, 78
- Lodders, K., & Fegley, B. 2002, *Icar*, **155**, 393
- Madhusudhan, N., Amin, M. A., & Kennedy, G. M. 2014, *ApJL*, **794**, L12
- Madhusudhan, N., & Seager, S. 2011, *ApJ*, **729**, 41
- McBride, B. J., Gordon, S., & Reno, M. A. 1993, *Coefficients for Calculating Thermodynamic and Transport Properties of Individual Species*, Technical Memorandum TM-4513 (Washington, D.C.: NASA)
- Morley, C. V., Fortney, J. J., Marley, M. S., et al. 2012, *ApJ*, **756**, 172
- Morley, C. V., Fortney, J. J., Marley, M. S., et al. 2015, *ApJ*, **815**, 110
- Moses, J. I., Line, M. R., Visscher, C., et al. 2013, *ApJ*, **777**, 34
- Moses, J. I., Visscher, C., Fortney, J. J., et al. 2011, *ApJ*, **737**, 15
- Müller-Wodarg, I. C. F., Yelle, R. V., Mendillo, M., Young, L. A., & Aylward, A. D. 2000, *JGR*, **105**, 20833
- Öberg, K. I., Murray-Clay, R., & Bergin, E. A. 2011, *ApJL*, **743**, L16
- Parmentier, V., Fortney, J. J., Showman, A. P., Morley, C., & Marley, M. S. 2016, *ApJ*, **828**, 22
- Parmentier, V., & Guillot, T. 2014, *A&A*, **562**, A133
- Parmentier, V., Guillot, T., Fortney, J. J., & Marley, M. S. 2015, *A&A*, **574**, A35
- Radhakrishnan, K., & Hindemarch, A. C. 1993, *NASRP*, 1327, UCRL-ID-113855
- Rieke, G. H., Wright, G. S., Boker, T., et al. 2015, *PASP*, **127**, 584
- Rothman, L. S., Gordon, I. E., Barber, R. J., et al. 2010, *JQSRT*, **111**, 2139
- Rothman, L. S., Gordon, I. E., Babikov, Y., et al. 2013, *JQSRT*, **130**, 4
- Rugheimer, S., Kaltenecker, L., Segura, A., Linsky, J., & Mohanty, S. 2015, *ApJ*, **809**, 57
- Rugheimer, S., Kaltenecker, L., Zsom, A., Segura, A., & Sasselov, D. 2013, *AsBio*, **13**, 251
- Seager, S., & Sasselov, D. D. 2000, *ApJ*, **537**, 916
- Showman, A. P., Fortney, J. J., Lian, Y., et al. 2009, *ApJ*, **699**, 564
- Sing, D. K., Fortney, J. J., Nikolov, N., et al. 2016, *Natur*, **529**, 59
- Stevenson, K. B., Lewis, N. K., Bean, J. L., et al. 2016, *PASP*, **128**, 094401
- Triaud, A. H. M. J., Gillon, M., Ehrenreich, D., et al. 2015, *MNRAS*, **450**, 2279
- Venot, O., Hébrard, E., Agúndez, M., et al. 2012, *A&A*, **546**, A43
- Venot, O., Rochetto, M., Carl, S., Roshni Hashim, A., & Decin, L. 2016, *ApJ*, **830**, 77
- Wakeford, H. R., & Sing, D. K. 2015, *A&A*, **573**, A122
- Wakeford, H. R., Sing, D. K., Kataria, T., et al. 2017, *Sci*, **356**, 628
- Wong, M. H., Mahaffy, P. R., Atreya, S. K., Niemann, H. B., & Owen, T. C. 2004, *Icar*, **171**, 153
- Yelle, R. V. 2004, *Icar*, **170**, 167
- Zahnle, K., Marley, M. S., Freedman, R. S., Lodders, K., & Fortney, J. J. 2009, *ApJL*, **701**, L20
- Zahnle, K., Marley, M. S., Morley, C. V., & Moses, J. I. 2016, *ApJ*, **824**, 137
- Zahnle, K. J., & Marley, M. S. 2014, *ApJ*, **797**, 41